

### Supporting Information

## The Electrochemical Reduction of a Flexible Mn(II) Salen-Based Metal-Organic Framework

Marcello B. Solomon,<sup>a</sup> Carol Hua,<sup>b</sup> Bun Chan,<sup>c</sup> Tamara L. Church,<sup>d</sup> Seth M. Cohen,<sup>e</sup> Clifford P. Kubiak,<sup>e</sup> Katrina A.

Jolliffe<sup>a</sup> and Deanna M. D'Alessandro<sup>\*a</sup>

### Acknowledgements

This project was supported by the Science and Industry Endowment Fund (SIEF) as part of the 'Solving the Energy Waste Roadblock' venture, and by a Commonwealth Scientific and Industrial Research Organisation (CSIRO) OCEPhD scholarship. We are grateful to Dr. Danielle Kennedy at the CSIRO for her support in the provision of an OCE PhD top-up scholarship for MBS. CH gratefully acknowledges the University of Melbourne for a McKenzie Fellowship. BC acknowledges the support of the Tokyo Ohka Foundation and the provision of computational resources from RIKEN Office for Information Systems and Cybersecurity. Some of this work was supported by the National Science Foundation, Division of Chemistry, under award number CHE-1661655.

### Table of Contents

Previously Reported Surface Areas of Salen-based MOFs.....	S2
General.....	S3
Synthesis of [Zn <sub>3</sub> (bpdc) <sub>3</sub> (L)].....	S4
Thermogravimetric Analysis (TGA).....	S5
Crystallography.....	S6
Powder X-Ray Diffraction (PXRD) and Framework Activation .....	S9
Computational Modelling of the Zn(II) Trimer.....	S11
Gas Sorption.....	S13
[Zn <sub>3</sub> (bpdc) <sub>3</sub> (L)] Crystallisation on Fluorine-doped Tin Oxide (FTO) Electrodes.....	S15
Electrochemistry.....	S16
References.....	S22

## Previously Reported Surface Areas of Salen-based MOFs

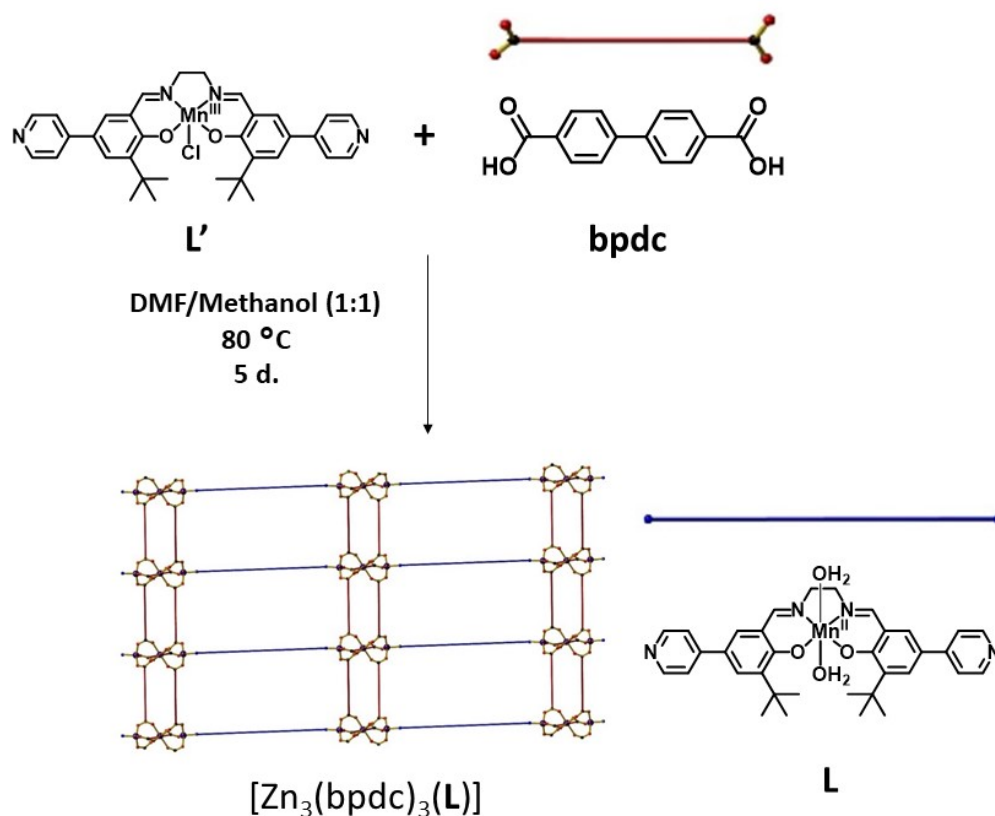
Table S1: Reported BET Surface Areas of Salen-based MOFs in the literature.

MOF Material	BET Surface Area (m <sup>2</sup> g <sup>-1</sup> )	Reference
Ps-CMOF	1088	1
[Zn <sub>3</sub> (bpdc) <sub>3</sub> (L)]	<b>967</b>	This Work
[Cd <sub>2</sub> (FeL <sub>2</sub> ) <sub>2</sub> O(BPDC) <sub>2</sub> ]	923	2
[Zn <sub>2</sub> (FeL <sub>1</sub> ) <sub>2</sub> O(BPDC) <sub>1.5</sub> ]	357	
[Cd <sub>2</sub> (VOL) (CuL)]	690	3
[Cd <sub>2</sub> (VOL) <sub>2</sub> ]	628	
M'MOF-4a	602	4
M'MOF-6a	369	
M'MOF-5a	202	
M'MOF-7a	90	
[Cd <sub>2</sub> (MnL <sup>1</sup> ) <sub>2</sub> (VOL <sup>2</sup> )]	584	5
[Cd <sub>2</sub> (FeL <sup>1</sup> ) <sub>2</sub> (VOL <sup>2</sup> ) <sub>2</sub> ]·(DMF) <sub>2</sub>	364	
V-salen Cd-bpdc MOF	574	6
ZSF-1	419	7
ZSF-2	355	
ZSF-3	422	
ZSF-4	359	
Cd <sub>2</sub> (Cu(salen))(DMF) <sub>3</sub>	421	8
Cd <sub>2</sub> (Ni(salen))(DMF) <sub>3</sub>	418	9
[Zn <sub>2</sub> (VOL <sup>1</sup> ) <sub>2</sub> ]	382	10
[Cd <sub>2</sub> (VOL <sup>2</sup> ) <sub>2</sub> (BPDC) <sub>2</sub> ]	288	
[Zn <sub>2</sub> (Fe-L) <sub>2</sub> (μ <sub>2</sub> -O)(H <sub>2</sub> O) <sub>2</sub> ]	270	11
[Cd <sub>2</sub> (Fe-L) <sub>2</sub> (μ <sub>2</sub> -O)(H <sub>2</sub> O) <sub>2</sub> ]	99	
MnSO-MOF	260	12
[Cd <sub>2</sub> (Ni-L) <sub>2</sub> (H <sub>2</sub> O) <sub>4</sub> ]	245	13
[Cd <sub>4</sub> (CuL) <sub>4</sub> (DMF) <sub>4</sub> ]	196	14

## General

Chemicals used were purchased from Aldrich, Alfa Aesar and Merck, and were used without further purification unless otherwise stated. The *tetrakis*(triphenylphosphine) palladium(0) catalyst [Pd(PPh<sub>3</sub>)<sub>4</sub>] was synthesised from palladium(II) chloride (Precious Metals Online) according to the literature procedure.<sup>15</sup> 3,3'-[1,2-Ethanediybis(nitromethylidene)]-*bis*[3-*tert*-butyl-2-hydroxy-5-(4-pyridinyl)-benzaldehyde] manganese(III) chloride (**L**) was synthesised according to literature techniques, with all characterisation data matching that reported.<sup>16</sup> Room temperature FTIR spectra were obtained using a PerkinElmer UATR 2 infrared spectrometer over the range 400–4000 cm<sup>-1</sup> with a resolution of 4 cm<sup>-1</sup>. Solid state UV-Vis-NIR spectra were obtained over the range of 5000–40000 cm<sup>-1</sup> using a CARY5000 Spectrophotometer with a Praying Mantis™ accessory interfaced to Varian WinUV software. The baseline was first measured using KBr. The diffuse reflectance UV-Vis-NIR spectra of the redox-active species were collected *in situ* using a CARY5000 UV-Vis-NIR spectrophotometer equipped with a Harrick Omni Diff Probe attachment interfaced to Varian WinUV software over the range 5000–25000 cm<sup>-1</sup> in a custom-made cell previously reported by D'Alessandro *et al.*<sup>17</sup> The cell consisted of a Pt wire counter electrode and a Ag/Ag<sup>+</sup> *quasi*-reference electrode. The solid sample was immobilised by a thin strip of Teflon tape onto a 0.1-mm thick Indium-doped Tin Oxide (ITO) coated quartz slide, which functioned as the working electrode. The applied potential was controlled using an eDAQ 410 potentiostat. Continuous scans of the sample were obtained and the potential increased gradually until a change in the spectrum was observed. Microanalyses of novel salen compounds were carried out by Dr Christopher McRae at the Chemical Analysis Facility – Elemental Analysis Service in the Department of Chemistry and Biomolecular Science at Macquarie University, Australia. Topological analysis of the networks was performed by Dr Carol Hua using the program package ToposPro, where the Zn(II) node was determined to be 8-c and the ligands treated as 2-c linkers.<sup>18</sup>

## Synthesis of $[\text{Zn}_3(\text{bpdc})_3(\text{L})]$



Scheme S1: Synthesis of  $[\text{Zn}_3(\text{bpdc})_3(\text{L})]$ .

$\text{Zn}(\text{NO}_3)_2 \cdot 6\text{H}_2\text{O}$  (6.0 mg, 32  $\mu\text{mol}$ ),  $\text{L}'$  (16 mg, 26  $\mu\text{mol}$ ) and bpdc (3.6 mg, 15  $\mu\text{mol}$ ) were dissolved in DMF/MeOH (1:1, 3 mL) and heated at 80  $^\circ\text{C}$  for 5 d, upon which dark yellow block crystals were formed. The crystals were then washed several times with DMF/Methanol (1:1 v/v) to yield the framework (Yield: 12 mg, 52%).

**ATR-IR** ( $\text{cm}^{-1}$ )  $\nu_{\text{O-C(Ph)}}$  = 1656,  $\nu_{\text{C=N}}$  = 1604 **UV-Vis-NIR**  $\lambda(\text{KBr}, \text{cm}^{-1})$  15640, 20470(sh), 23520(sh), 27160, 31690

**Elemental Analysis** calculated for  $\text{C}_{76}\text{H}_{62}\text{MnN}_4\text{O}_{15}\text{Zn}_3 \cdot 2\text{H}_2\text{O} \cdot 5\text{MeOH} \cdot 3\text{DMF}$ : C 55.78, H 5.57, N 5.06%, found C 56.10, H 5.74, N 5.19%

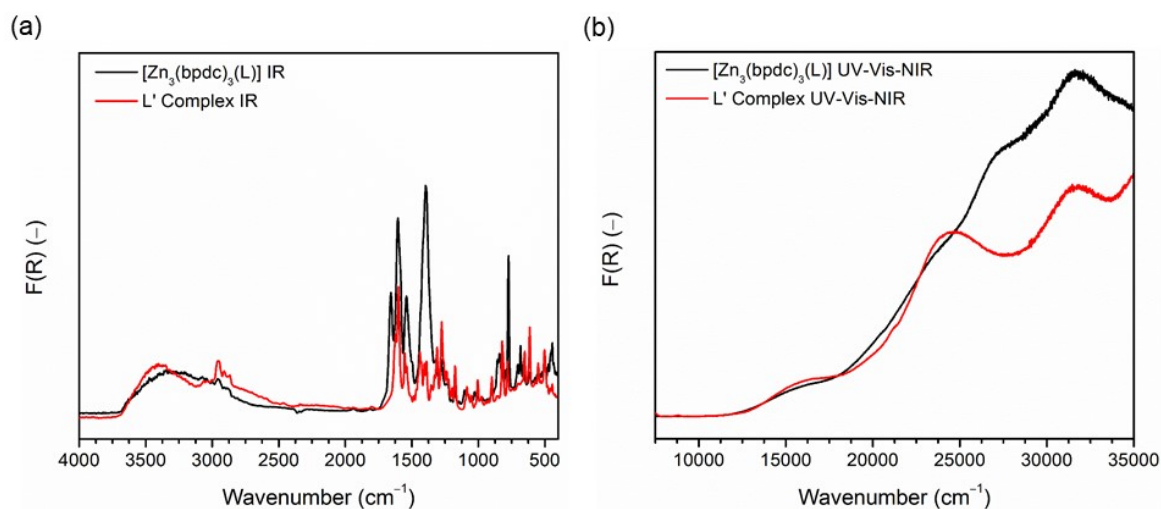


Figure S1: **(a)** Solid-state FTIR and **(b)** UV-Vis-NIR spectra of  $[\text{Zn}_3(\text{bpdc})_3(\text{L})]$  (black) and discrete complex  $\text{L}'$  (red).

## Thermogravimetric Analysis (TGA)

TGA measurements were carried out on a TA Instruments Hi-Res 2950 Thermogravimetric Analyser. Dry N<sub>2</sub> (0.1 L min<sup>-1</sup>) flowed during data collection. In order to identify the approximate temperatures of guest loss and thermal decomposition, the was heated at 1 °C min<sup>-1</sup> from 25 to 700 °C. The sample was loaded dry after exposure to air.

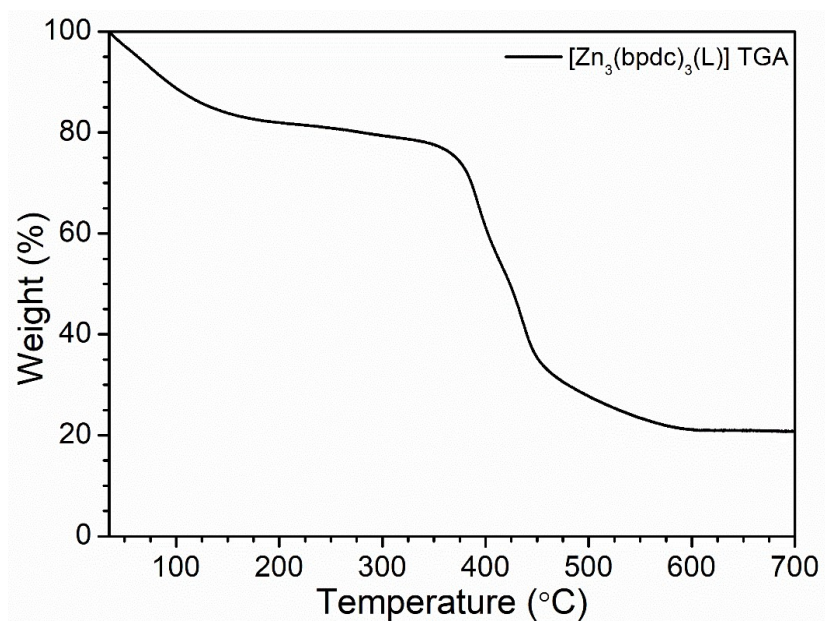


Figure S2: TGA of [Zn<sub>3</sub>(bpdc)<sub>3</sub>(L)].

## Crystallography

A yellow block-like crystal was mounted on a SuperNova Atlas diffractometer employing mirror monochromated CuK $\alpha$  radiation generated from a micro-focus sealed X-ray tube. Cell constants were obtained from a least squares refinement against 13507 reflections located between  $2\theta = 7.40$  and  $131.52^\circ$ . Data was collected at 150(2) K with  $\phi$  and  $\omega$  scans to  $149.13^\circ 2\theta$ . The structure was solved using intrinsic phasing with SHELXT<sup>19</sup>, and refined with SHELXL<sup>20</sup> within the Olex2 graphical interface.<sup>21</sup>

The structure was solved in the monoclinic space group  $C2/c$ . The non-hydrogen atoms in the asymmetric unit were modelled with anisotropic displacement parameters. A riding-atom model was used for all hydrogen atoms. A two-fold disorder exists for half of the salen ligand. The diffuse electron density due to the disordered solvent molecules within the pores of  $[Zn_3(bpdc)_3(L)]$  was treated using the solvent mask in Olex2, which yielded 1912 e<sup>-</sup>/void.

Table S2: Analysis of the possible coordination geometries for Mn1 and Zn2 using the SHAPE program<sup>22</sup>. Values indicate the deviation of from the ideal coordination geometry. Minima are indicated in bold.

Geometry	Symmetry	Mn1	Zn2
Hexagon	D <sub>6h</sub>	30.619	31.360
Pentagonal pyramid	C <sub>5v</sub>	27.080	28.895
Octahedron	O <sub>h</sub>	<b>1.696</b>	<b>0.063</b>
Trigonal prism	D <sub>3h</sub>	15.462	15.953
Johnson pentagonal pyramid 32	C <sub>5v</sub>	29.909	32.363

Table S3: Analysis of the possible coordination geometries for Zn1 and Zn3 using the SHAPE program<sup>22</sup>. Values indicate the deviation of from the ideal coordination geometry. Minima are indicated in bold.

Geometry	Symmetry	Zn1	Zn3
Square	D <sub>4h</sub>	30.235	32.788
Tetrahedron	T <sub>d</sub>	<b>0.838</b>	<b>0.595</b>
Seesaw	C <sub>2v</sub>	6.220	7.993
Vacant trigonal bipyramid	C <sub>3v</sub>	1.519	1.359

Table S4: Crystal data and structure refinement details for [Zn<sub>3</sub>(bpdc)<sub>3</sub>(L)].

	[Zn <sub>3</sub> (bpdc) <sub>3</sub> (L)]
Formula	C <sub>76</sub> H <sub>62</sub> MnN <sub>4</sub> O <sub>15</sub> Zn <sub>3</sub>
M/ (g mol <sup>-1</sup> )	1522.34
Temperature (K)	150(2)
Crystal system	Monoclinic
Space Group	<i>C2/c</i>
Crystal size (mm <sup>3</sup> )	0.06 × 0.05 × 0.02
Crystal Colour	Yellow
Crystal Habit	Block
<i>a</i> (Å)	65.1518(10)
<i>b</i> (Å)	14.7217(2)
<i>c</i> (Å)	24.4314(4)
$\beta$ (°)	110.1980(10)
<i>V</i> (Å <sup>3</sup> )	21992.2(6)
<i>Z</i>	8
$\rho_{\text{calc}}$ (mg mm <sup>-3</sup> )	0.920
$\lambda$ (CuK $\alpha$ ) (Å)	1.54178 Å
$\mu$ (CuK $\alpha$ ) (mm <sup>-1</sup> )	2.022 mm <sup>-1</sup>
Reflections collected	141873/22242 [ <i>R</i> <sub>merge</sub> = 0.1215, <i>R</i> <sub>sigma</sub> = 0.0840]
Data/parameters	22242/838
Final <i>R</i> indexes [ <i>I</i> ≥ 2σ( <i>I</i> )]	<i>R</i> <sub>1</sub> = 0.0854, <i>wR</i> <sub>2</sub> = 0.2385
Final <i>R</i> indexes [all data]	<i>R</i> <sub>1</sub> = 0.1402, <i>wR</i> <sub>2</sub> = 0.2798
Goodness-of-fit on <i>F</i> <sup>2</sup>	0.966
Largest diff. peak/hole (e <sup>-</sup> Å <sup>-3</sup> )	-1.04, 1.75

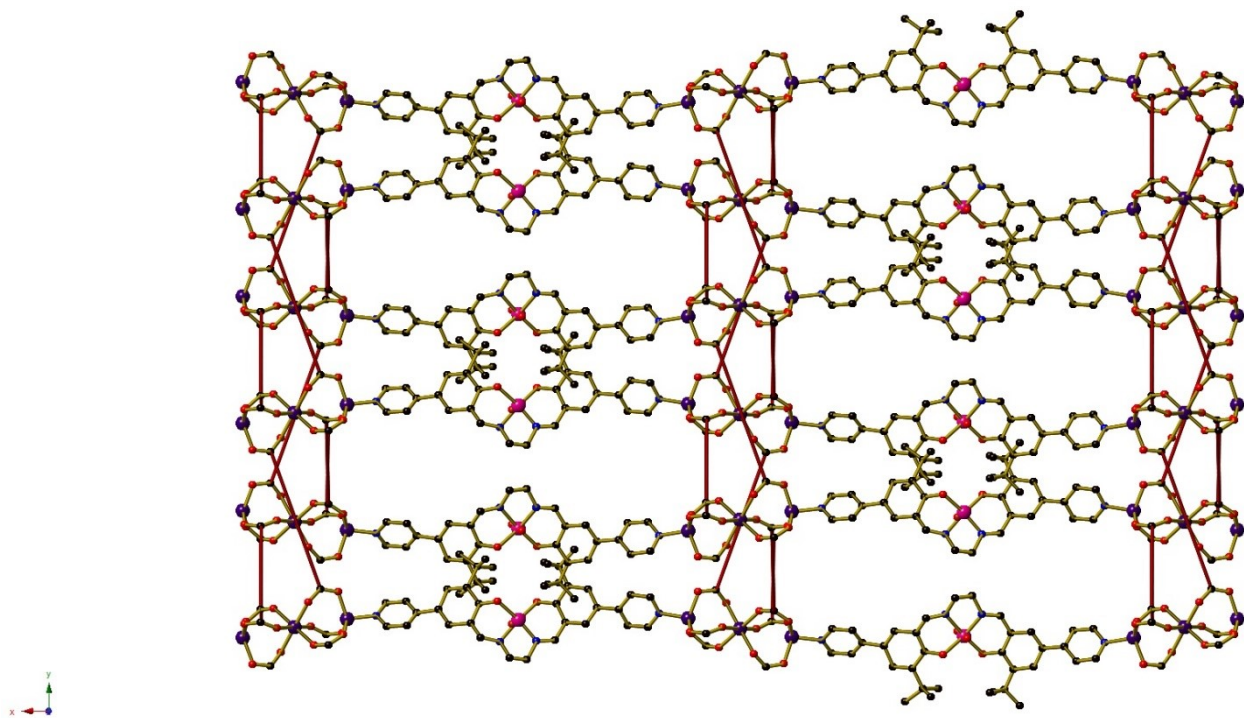


Figure S3: Visualisation of  $[Zn_3(bpdc)_3(L)]$  showing the accessible salen metal complexes.

## Powder X-Ray Diffraction (PXRD) and Framework Activation

PXRD data was collected over the  $2\theta = 5\text{--}50^\circ$  with a  $0.02^\circ$  step size and  $2^\circ\text{min}^{-1}$  scan rate on a PANalytical X'Pert Pro diffractometer fitted with a solid-state PIXcel detector (45 kV, 40 mA,  $1^\circ$  divergence and anti-scatter slits, and 0.3 mm receiver and detector slits) using Cu-K $\alpha$  ( $\lambda = 1.5406 \text{ \AA}$ ) radiation. The sample was first loaded dry (2 mg) for flat plate measurements; however, once it was discovered that the desolvated mode was amorphous (Figure S4a), samples were loaded into 0.5-mm glass capillaries. Samples were left solvated in the capillaries, or desolvated overnight on a Schlenk line at  $70^\circ\text{C}$  prior to measurements. Fresh solvent was added to the desolvated capillary and was allowed to stand overnight prior to re-measurement.

Activation of the MOF was achieved by solvent exchange using methanol. The MOF was exposed to various solvents, and retained its crystallinity upon exposure to alcohols. The framework was unstable to solvent exchange with acetonitrile, chlorinated solvents and water (Figure S5b). The MOF was activated through washing *via* a Soxhlet washing procedure<sup>23</sup> in methanol for 2 d. The crystals were dried *in vacuo* overnight at  $80^\circ\text{C}$ . To show that the sample maintained its crystallinity following gas sorption analysis, the sample was suspended in methanol (Figure S5c).

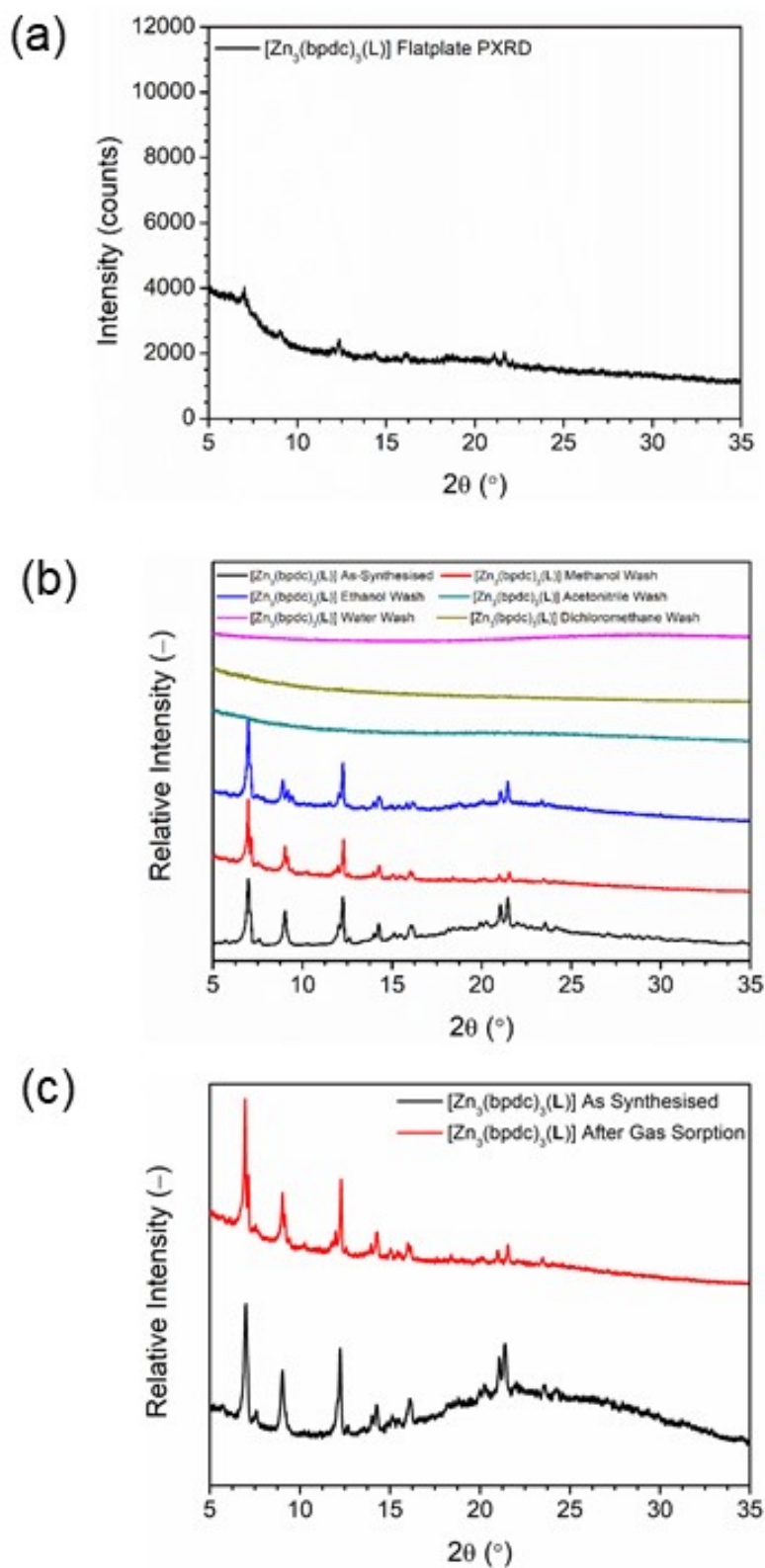


Figure S4: PXR D of **(a)**  $[\text{Zn}_3(\text{bpdc})_3(\text{L})]$  measured in flat plate mode **(b)**  $[\text{Zn}_3(\text{bpdc})_3(\text{L}')$  after washing with DMF (black), MeOH (red), EtOH (blue), MeCN (green), DCM (yellow) and  $\text{H}_2\text{O}$  (pink) and **(c)** before (black) and after (red) gas sorption measurements.

## Computational Modelling of the Zn(II) Trimer

Standard computational chemistry calculations were carried out with Gaussian 16.<sup>24</sup> The initial geometries for the Zn(II) trimer moiety were obtained from the crystal structure, largely without re-optimisation. To simplify the model, formate moieties were used in place of the bridging bpdc<sup>2-</sup> ligand, while the trimer was capped with pyridine moieties in place of the salen metal complex (Figure S5). The coordinates of the formate and pyridine moieties were optimised with the PM6 method.<sup>25</sup> The Zn(II) trimer structure was then fully optimised at the B3LYP/def2-SVP level.<sup>26,27</sup> Single-point energies were obtained with the MN15/ma'-def2-TZVP method,<sup>28</sup> where the ma' prefix for the basis set indicates the inclusion of a minimal set of diffuse functions for electronegative elements (N and O).

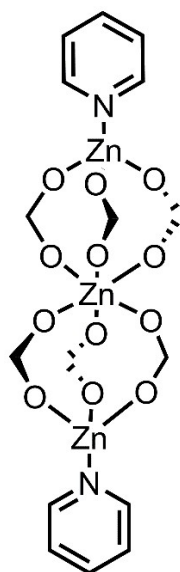
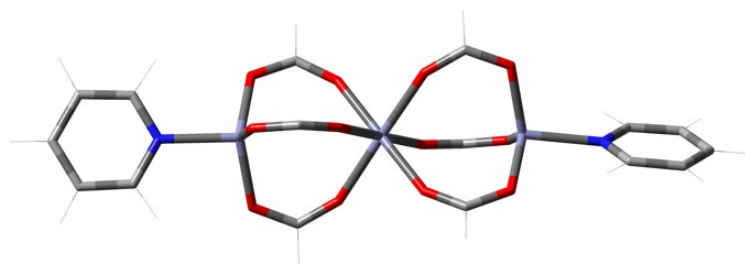
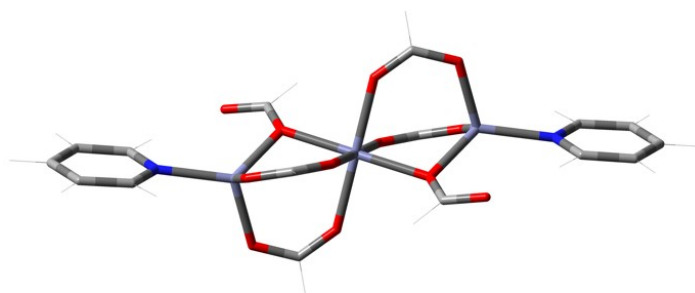


Figure S5: The Zn(II) trimer used for modelling studies

The framework undergoes reversible transformation between crystalline and amorphous structures upon desolvation. Given that the salen metal complex and bpdc are both flexible, it is possible that the MOF contorts upon changes in the secondary building unit (SBU). The geometries of the model Zn(II) trimer were optimised following the removal of solvent molecules. Three key structures were obtained (Figure S6), two of which possessed Zn–O–Zn bridges, in addition to the typical Zn–OCO–Zn bridges. The Zn–O–Zn bridges, formed from the potential rotation of the carboxylate moiety, lower the energy of the trimer. In particular, the formation of the zinc trimer containing two Zn–O–Zn bridges and four Zn–OCO–Zn bridges (Figure S6b) is lower in energy than the original SBU containing six Zn–OCO–Zn bridges (Figure S6a) by 27 kJ mol<sup>-1</sup>. This thermodynamic driving force, combined with the flexibility of both framework ligands, may facilitate the reversible crystalline-to-amorphous transition. Although a trimer containing four Zn–O–Zn bridges and two Zn–OCO–Zn bridges was obtained (Figure S6c), the relative energy of this trimer is higher than that of the original SBU.



(a)  $0 \text{ kJ mol}^{-1}$



(b)  $-27 \text{ kJ mol}^{-1}$



(c)  $+17 \text{ kJ mol}^{-1}$

Figure S6. Structural isomers of the model Zn(II) trimer and their relative energies.

## Gas Sorption

Adsorption isotherms were measured using an Accelerated Surface Area & Porosity (ASAP) 2020 instrument, supplied by Micromeritics Instruments Inc. The sample was loaded into a glass analysis tube and outgassed for 24 h under vacuum at 80 °C prior to analysis. The activated sample weighed 40.9 mg. N<sub>2</sub> and H<sub>2</sub> isotherms (adsorption and desorption) were measured at 77 K, and data were analysed using the Brunauer, Emmett and Teller (BET) model to determine the surface area.<sup>29</sup> Pore size distributions were calculated using the non-local Density Functional Theory (DFT) cylindrical oxide model in the Micromeritics MicroActive Software Package, Version 4.03. The data was based on the N<sub>2</sub> adsorption data.

Low-pressure CO<sub>2</sub> measurements (up to 1 bar) were carried out at three temperatures (298, 308 and 318 K) on the ASAP2020. The data were modelled using a virial equation before applying the Clausius–Clapeyron relation (1).

$$(\ln P)_n = - \left( \frac{Q_{st}}{R} \right) \left( \frac{1}{T} \right) + C \quad (1)$$

(P = pressure (mbar), n = amount of gas adsorbed (mol mol<sup>-1</sup>), T = temperature (K), R = universal gas constant (J mol<sup>-1</sup> K<sup>-1</sup>) and C = constant).

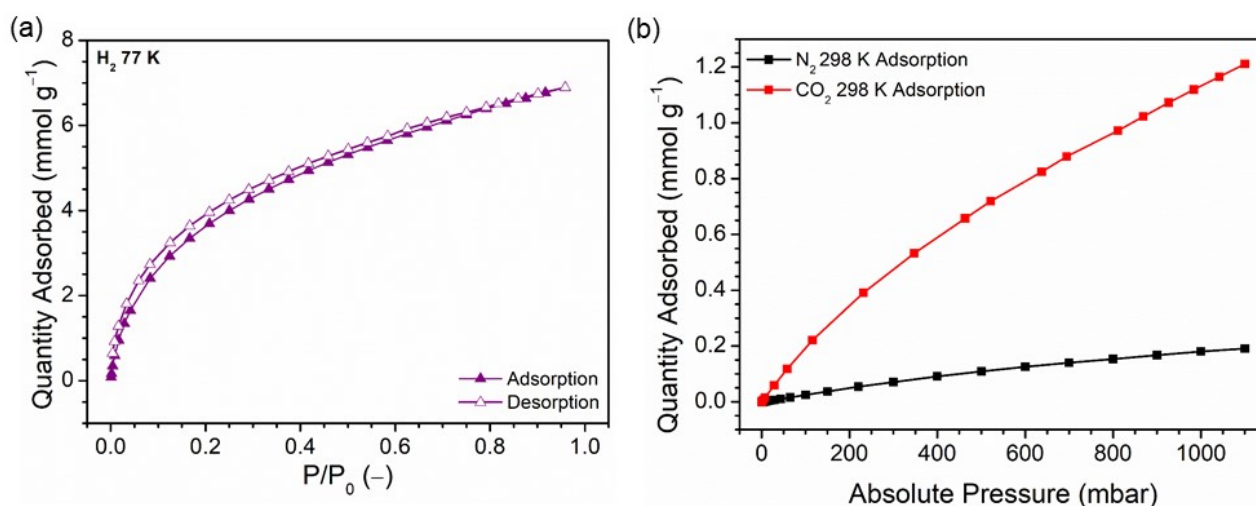


Figure S7: **(a)** H<sub>2</sub> isotherms measured at 77 K of [Zn<sub>3</sub>(bpdc)<sub>3</sub>(L)]. **(b)** N<sub>2</sub> (black) and CO<sub>2</sub> (red) isotherms of [Zn<sub>3</sub>(bpdc)<sub>3</sub>(L)], measured at 298 K. Filled and empty shapes represent adsorption and desorption isotherms, respectively.

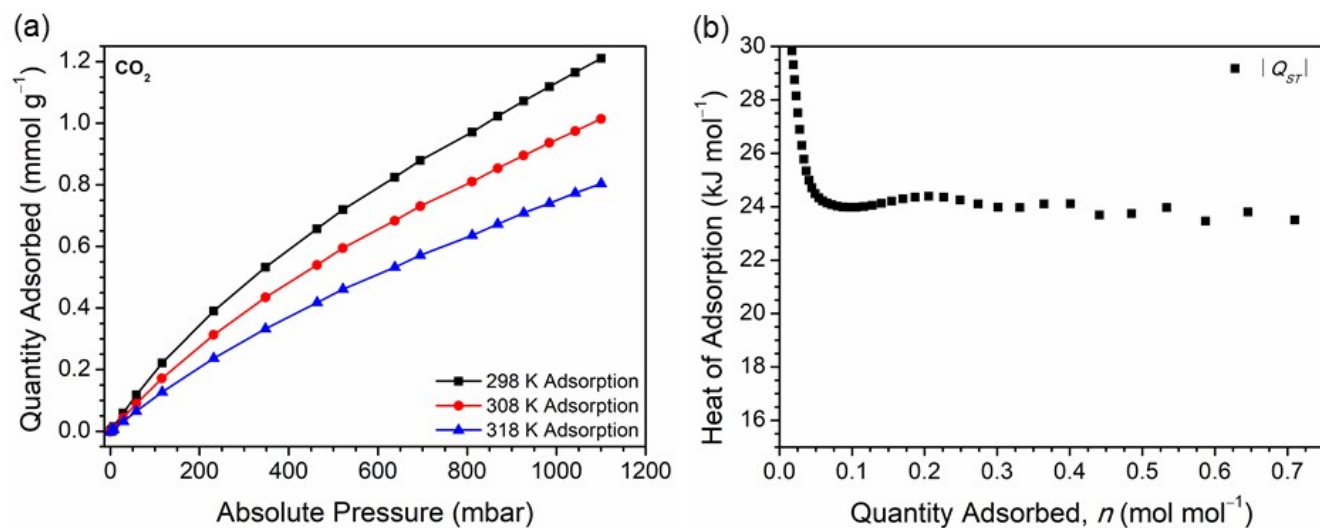


Figure S8: **(a)** CO<sub>2</sub> adsorption isotherms of [Zn<sub>3</sub>(bpdc)<sub>3</sub>(L)] at 298 K (black), 308 K (red) and 318 K (blue). Desorption isotherms are not shown for clarity. **(b)** Isosteric heats of adsorption for [Zn<sub>3</sub>(bpdc)<sub>3</sub>(L)].

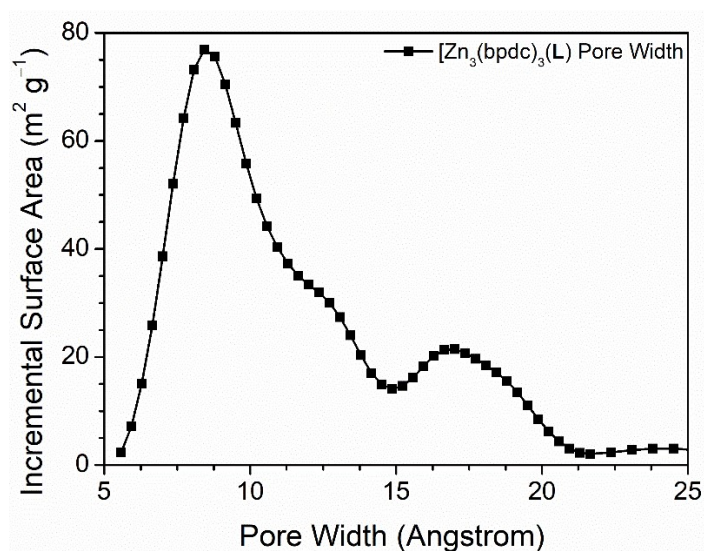


Figure S9: Pore size distributions of [Zn<sub>3</sub>(bpdc)<sub>3</sub>(L)].

## [Zn(bpdc)(L)] Crystallisation on Fluorine-doped Tin Oxide (FTO) Electrodes

FTO glass substrates were cut into smaller pieces for coating ( $3\text{ cm} \times 1\text{ cm}$ ). Prior to the crystallisation of  $[\text{Zn}_3(\text{bpdc})_3(\text{L})]$  onto the FTO glass substrate, the substrate was activated through washing with water ( $5 \times 2\text{ mL}$ ) and methanol ( $5 \times 2\text{ mL}$ ) then dried for 20 min. The activated FTO substrate was then immersed in a solution of bpdc in DMF (1 mM, 6 mL) for 24 h to install anchoring sites on the surface of the FTO for the crystallisation of  $[\text{Zn}_3(\text{bpdc})_3(\text{L})]$ .

The  $[\text{Zn}_3(\text{bpdc})_3(\text{L})]$  films were prepared solvothermally. Prior to heating, the treated FTO glass substrate was immersed in a solution of the reaction mixture and heated at  $80\text{ }^\circ\text{C}$  for 5 d. The films were washed with fresh synthesis solvent, then stored in solvent.

Field Emission Scanning Electron Microscopy (FE-SEM) measurements were obtained at the Nano3 facility at The University of California, San Diego. An  $[\text{Zn}_3(\text{bpdc})_3(\text{L})]$  electrode was adhered to conductive carbon tape on a sample holder disk. The disk was coated using a Cr sputter coating for 8 s. A Philips XL30 ESEM was used to acquire images using a 10-kV energy source under vacuum at a working distance at 10.9 mm.

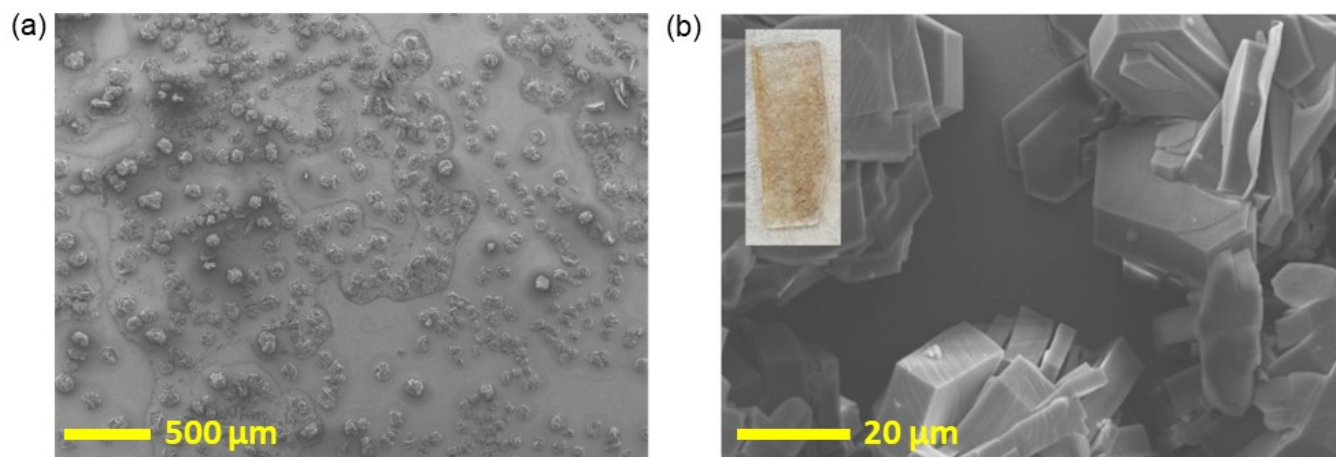


Figure S10: FE SEM images of  $[\text{Zn}_3(\text{bpdc})_3(\text{L})]$  at (a)  $36\times$  and (b)  $19000\times$  magnification. The inset in the top left corner of (b) is the image of the electrode surface.

## Electrochemistry

### General Experimental

Solution-state electrochemical measurements were performed using a Bioanalytical Systems BASi Epsilon Electrochemical Analyser. A single compartment cell was used, and consisted of a glassy carbon working electrode (3.0 mm diameter), a platinum wire auxiliary electrode and an electrolysed Ag/AgCl wire reference electrode separated from the solution by a CoralPor tip. Cyclic (CV) and differential pulse voltammograms (DPV) were performed using a solution of the analyte (1 mM complex in 0.1 M  $[(n\text{-C}_4\text{H}_9)_4\text{N}]\text{PF}_6$  in either MeCN or DMF, 10 mL). Prior to each experiment, the solution was purged with dried  $\text{N}_2$ . Ferrocene (Fc) (1 mM) was added as an internal standard during each experiment. All potentials are quoted in V vs.  $\text{Fc}^0/\text{Fc}^+$ . Uncompensated resistance between the working and the reference electrodes was corrected by using  $iR$  compensation on the potentiostat.

Solid-state electrochemical measurements were performed using a Bioanalytical Systems BASi Epsilon potentiostat. A single compartment cell with a three-electrode setup was used, consisting of an FTO electrode with immobilised  $[\text{Zn}_3(\text{bpdC})_3(\text{L})]$ , attached using a steel alligator clip to tinned copper wire, a platinum wire auxiliary electrode and a leakless Ag/AgCl reference electrode (eDAQ). CV measurements were performed using a solution of 0.1 M  $\text{LiBF}_4$  in DMF (10 mL). Prior to each experiment, the solution was purged with dried  $\text{N}_2$ . All potentials are quoted in V vs.  $\text{Fc}^0/\text{Fc}^+$ . Uncompensated resistance between the working and the reference electrodes was corrected by using  $iR$  compensation on the potentiostat. Scan-rate-dependence studies were measured at scan rates ranging from 25–1600  $\text{mVs}^{-1}$ . During CV measurements, the  $\text{Li}^+$  cations diffuse into the framework pores to balance the change in charge of the MOF.

### General Computational Details

Standard computational chemistry calculations were carried out with Gaussian 16.<sup>24</sup> The initial model geometries were obtained from the crystal structures, largely without re-optimisation. For the extended model compounds containing Zn(II) trimers, formats were added to complete the SBU. The coordinates of the formats were optimised using the PM6 method.<sup>25</sup> The structures for the Zn(II) trimers were fully optimised at the B3LYP/def2-SVP level.<sup>26</sup> <sup>27</sup> Single-point energies were obtained with the MN15/ma'-def2-TZVP method; the ma' prefix for the basis set indicates the inclusion of a minimal set of diffuse functions for electronegative elements (N and O).<sup>28</sup> Gas phase energies were further supplemented with solvation effects, computed with the SMD solvation model,<sup>30</sup> using parameters for DMF and densities obtained at the M05-2X/def2-SVP level.<sup>31</sup> A generic value of 5 V is assigned to the absolute reduction potential for the  $\text{Fc}^0/\text{Fc}^+$  redox couple.

## Co-ligand Electrochemistry

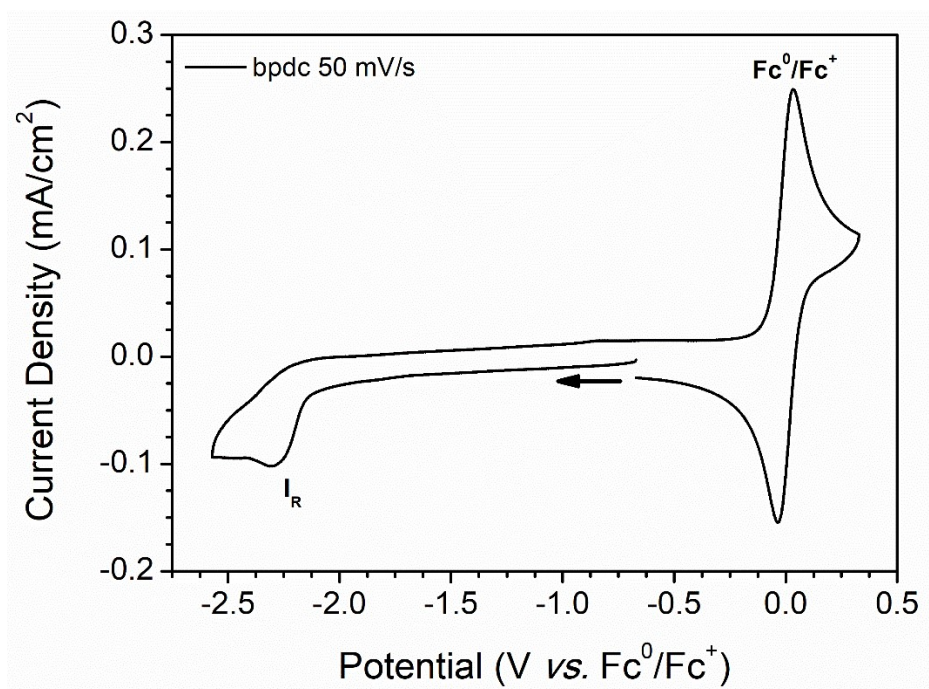


Figure S11: Solution state CV of bpdc (1 mM) 0.1 M  $[(n\text{-C}_4\text{H}_9)_4\text{N}]\text{PF}_6/\text{MeCN}$  as the supporting electrolyte under  $\text{N}_2$ , scan rate:  $0.05 \text{ V s}^{-1}$ , Fc (1 mM) was used as an internal standard.

## Electrochemistry Modelling

The experimental reduction of the salen metal complex in  $[\text{Zn}_3(\text{bpdc})_3(\text{L})]$  was explored by considering two models. One simulation was of the discrete Mn(II) salen metal complex, while the other simulation was the Mn(II) salen metal complex coordinated to two Zn(II) trimer SBUs (Figure S12). A neutral model, corresponding to Mn(II) in the central coordination sphere of the salen metal complex, was considered in both simulations.

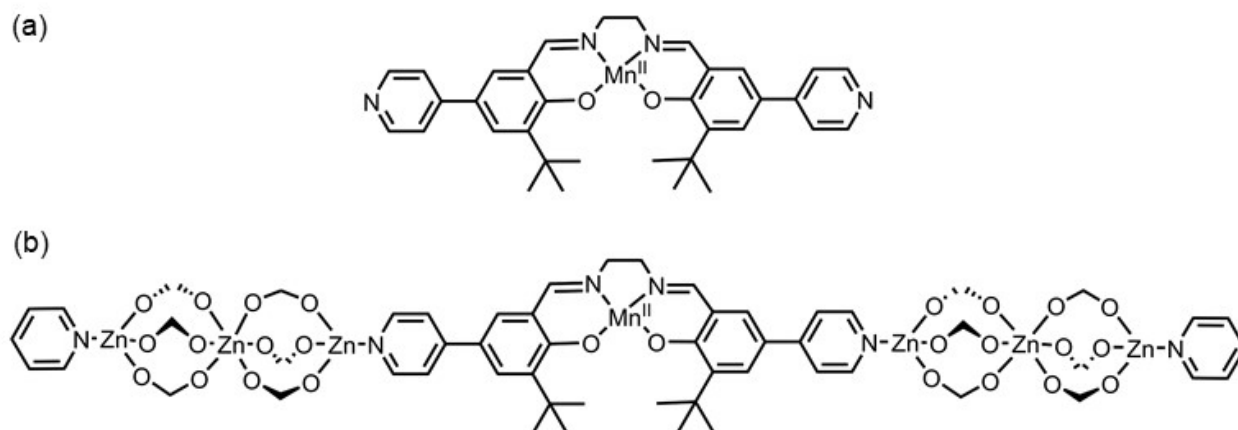


Figure S12. Models used for the computational study of salen electrochemistry.

Qualitative simulations were first performed to assign numeric values to the of the first electrochemical reductions. Studies on the discrete Mn(II) salen complex (Figure S12a) revealed a first reduction potential of  $-2.93$  V, which agrees well with the experimentally obtained result of  $-2.59$  V. When the Mn(II) salen complex is immobilised between two terminal Zn(II) trimer moieties (Figure S12b), the first reduction potential becomes more cathodic ( $-2.59$  V). The qualitative trend ( $-2.93$  V  $\rightarrow$   $-2.43$  V) is consistent with the experimental observation ( $-2.59 \rightarrow -1.57$  V).

Having analysed the qualitative reduction values of the models, studies turned to analysing the origins and nature of the reduction in  $[\text{Zn}_3(\text{bpdc})_3(\text{L})]$ . In a previous study, the reduction of a similar salen metal complex was attributed to the reduction of the ligand rather than the Mn metal centre by calculating spin densities.<sup>16</sup> Presently, the spin densities have been examined for the singly-reduced models. In both simulations, excess spins are observed on the salen backbone around the nitrile moiety, supporting a ligand-based reduction (Figure S13). For the discrete salen complex (Figure S12a), the excess spins on the ligand are more concentrated, which ultimately leads to a more unstable reduced species. In comparison, the coordination of Zn(II) trimers to the salen complex ((Figure S12b) suggests a more stable radical state and may account for the reason the redox process can be repeatedly in the MOF.

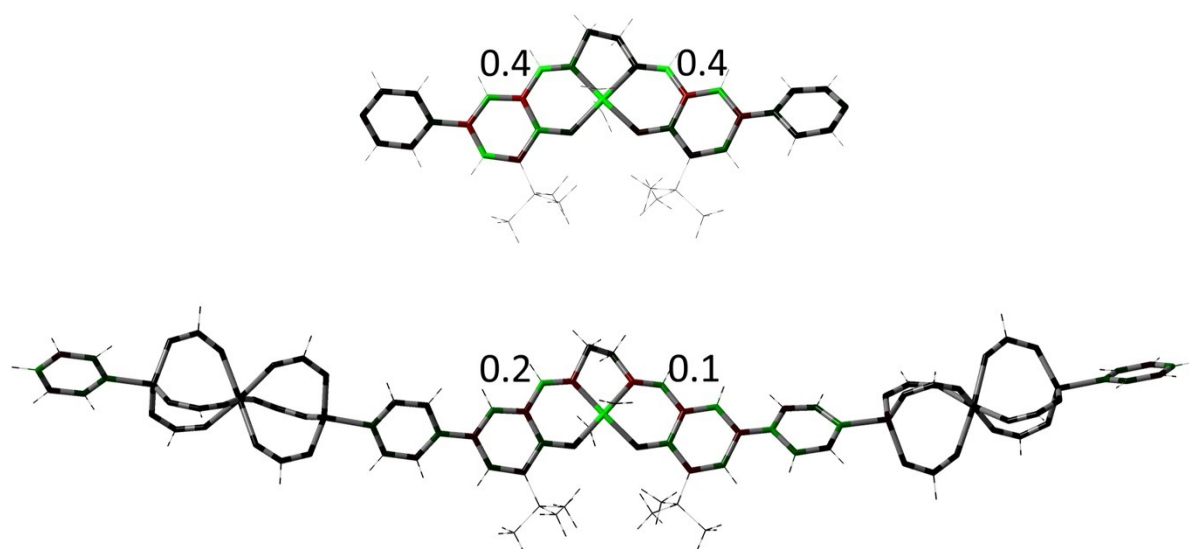


Figure S13. Depiction of spin density for the models in Figure S12. Green indicates net  $\alpha$ -spin. Also shown are values of a few key net  $\alpha$ -spins on the ligands.

Analysis of the  $I_R$  and  $II_R$  Reduction Processes

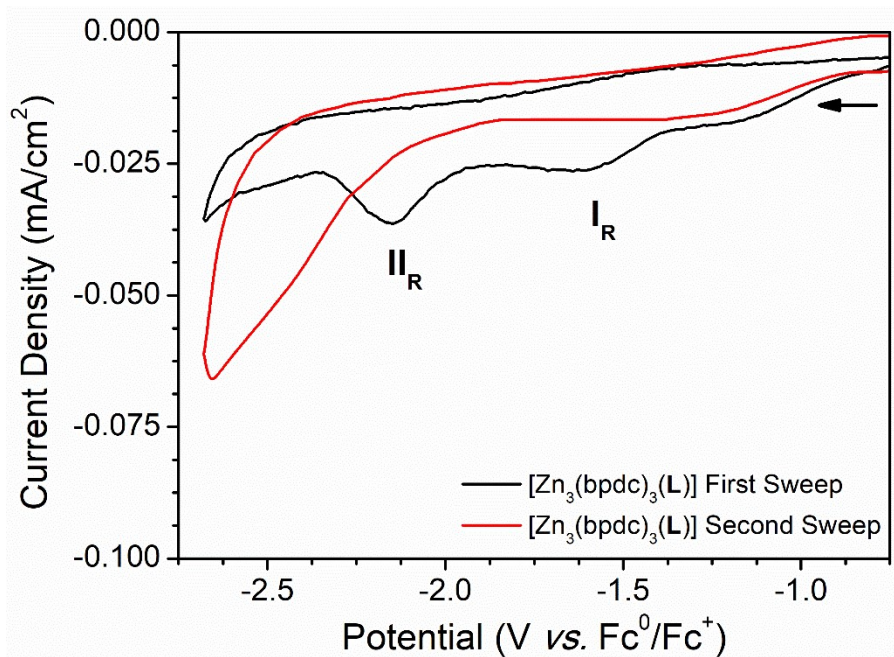


Figure S14: Solid state CV of [Zn<sub>3</sub>(bpdc)<sub>3</sub>(L)] at 0.025 V s<sup>-1</sup> after one (black) and two (red) anodic sweeps. The arrow indicates the direction of the sweep.

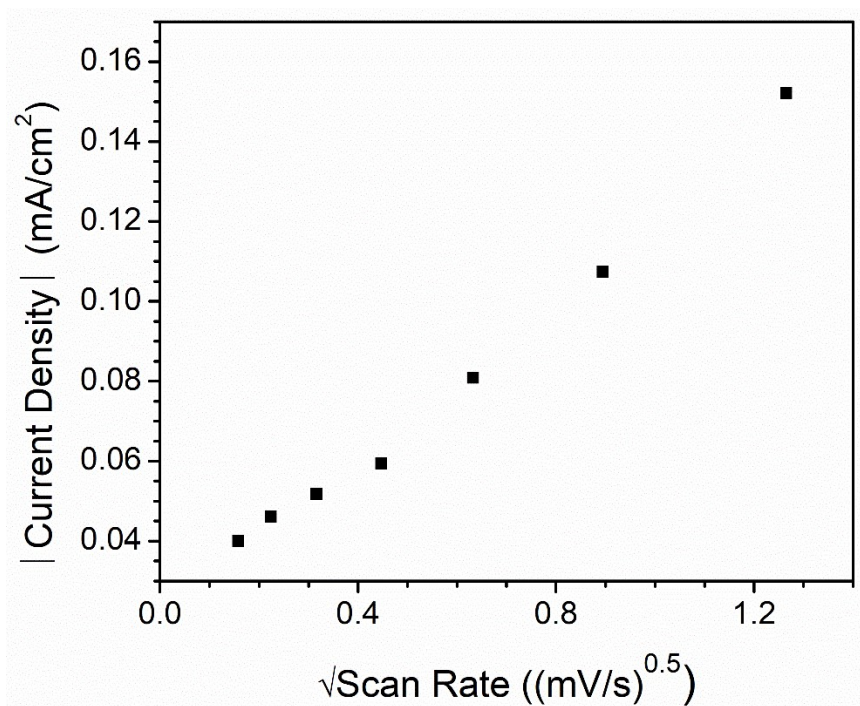


Figure S15: Scan Rate Dependence of the  $I_R$  process ( $E_{1/2} = -1.57$  V vs. Fc<sup>0</sup>/Fc<sup>+</sup>) of [Zn<sub>3</sub>(bpdc)<sub>3</sub>(L)].

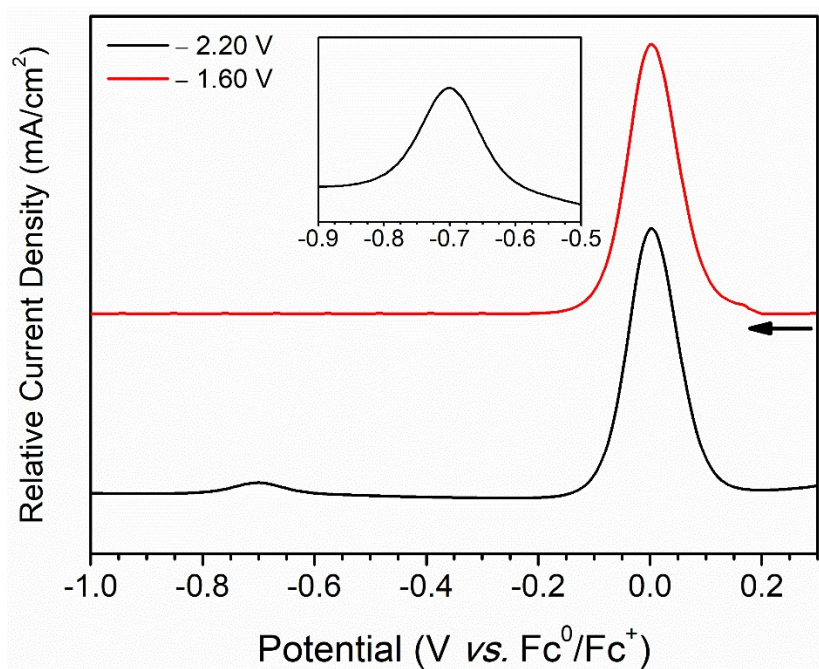


Figure S16: Solution-state DPV of the electrolyte solution formed after exposing  $[\text{Zn}_3(\text{bpd})_3(\text{L})]$ -modified FTO electrodes to constant potential electrolysis at  $-1.60$  (red) and  $-2.20$  V (black). The experiments were performed in  $0.1$  M  $\text{LiBF}_4/\text{DMF}$  that contained  $1$  mM  $\text{Fc}$  as an internal standard with a scan rate of  $0.025$  V  $\text{s}^{-1}$ . The data have been offset for clarity in the main figure.

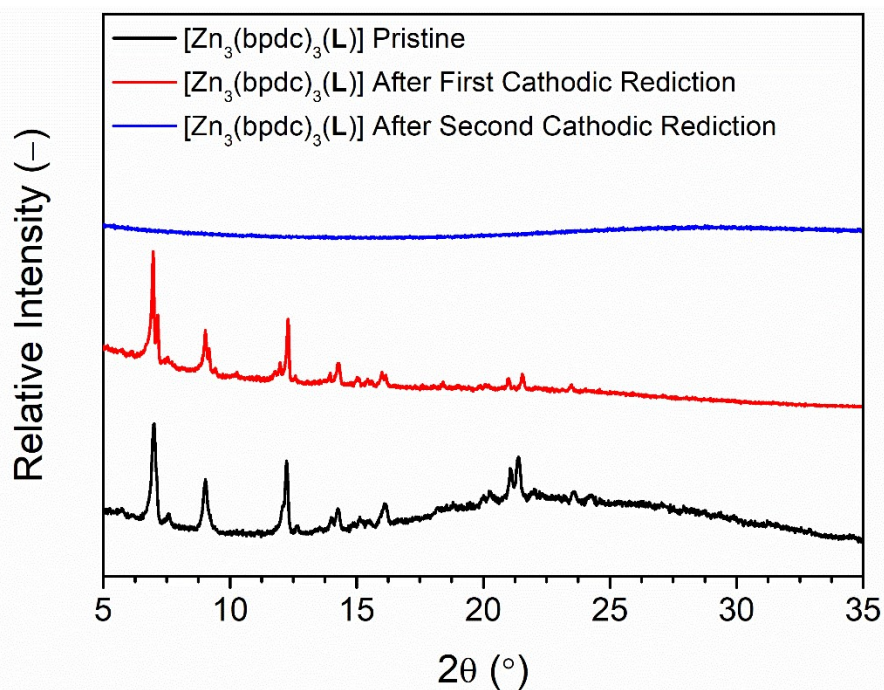


Figure S17: PXRD of  $[\text{Zn}_3(\text{bpd})_3(\text{L})]$  prior to electrochemical exposure (black), after exposure to the first cathodic reduction potential (red) and after exposure to the second reduction potential (blue).

### Ascribing the $\mathbf{II}_R$ reduction process

A controlled-potential electrolysis (CPE) experiment was performed on  $[\text{Zn}_3(\text{bpdc})_3(\mathbf{L})]$  at  $-2.20 \text{ V vs. Fc}^0/\text{Fc}^+$  (corresponding to  $\mathbf{II}_R$  in Figure S14) for 10 min. DPV measurements on the electrolyte following CPE showed a Gaussian peak at  $-0.70 \text{ V vs. Fc}^0/\text{Fc}^+$ . In the CV of the discrete complex, corresponding to the Mn(III/II) reduction. This suggests that some of this complex had been liberated from the MOF. DPV was used to quantify the leaching of manganese salen complex by comparing the area under the Mn redox process to that of a known concentration of Fc (1 mM) in solution. An  $\mathbf{L}$  concentration of  $55 \mu\text{mol}$  was calculated, indicating that 75% of the salen complex present in the  $[\text{Zn}_3(\text{bpdc})_3(\mathbf{L})]$ -functionalized FTO electrode was leaching into solution. Experimentally, it appears that a radical anion formation on the pyridyl moiety of the salen complex weakens the coordination of the salen complex to the Zn(II) trimer. The single-electron reduction  $\mathbf{I}_R$  does not appear to affect the integrity of the framework.

## References

1. J. Li, Y. Ren, C. Qi and H. Jiang, *Chem. Commun.*, 2017, **53**, 8223-8226.
2. Z. Yang, C. Zhu, Z. Li, Y. Liu, G. Liu and Y. Cui, *Chem. Commun.*, 2014, **50**, 8775-8778.
3. C. Zhu, Q. Xia, X. Chen, Y. Liu, X. Du and Y. Cui, *ACS Catal.*, 2016, **6**, 7590-7596.
4. M. C. Das, Q. Guo, Y. He, J. Kim, C.-G. Zhao, K. Hong, S. Xiang, Z. Zhang, K. M. Thomas, R. Krishna and B. Chen, *J. Am. Chem. Soc.*, 2012, **134**, 8703-8710.
5. Z. Li, Y. Liu, Q. Xia and Y. Cui, *Chem. Commun.*, 2017, **53**, 12313-12316.
6. A. Bhunia, S. Dey, J. M. Moreno, U. Diaz, P. Concepcion, K. Van Hecke, C. Janiak and P. Van Der Voort, *Chem. Commun.*, 2016, **52**, 1401-1404.
7. J. Li, Y. Ren, C. Yue, Y. Fan, C. Qi and H. Jiang, *ACS Appl. Mater. Interfaces*, 2018, **10**, 36047-36057.
8. Y. Fan, Y. Ren, J. Li, C. Yue and H. Jiang, *Inorg. Chem.*, 2018, **57**, 11986-11994.
9. Y. Fan, J. Li, Y. Ren and H. Jiang, *Eur. J. Inorg. Chem.*, 2017, **2017**, 4982-4989.
10. W. Xi, Y. Liu, Q. Xia, Z. Li and Y. Cui, *Chem. Eur. J.*, 2015, **21**, 12581-12585.
11. J. Li, J. Yang, Y.-Y. Liu and J.-F. Ma, *Chem. Eur. J.*, 2015, **21**, 4413-4421.
12. A. M. Shultz, O. K. Farha, D. Adhikari, A. A. Sarjeant, J. T. Hupp and S. T. Nguyen, *Inorg. Chem.*, 2011, **50**, 3174-3176.
13. Y. Ren, Y. Shi, J. Chen, S. Yang, C. Qi and H. Jiang, *RSC Adv.*, 2013, **3**, 2167-2170.
14. Y. Liu, Z. Li, G. Yuan, Q. Xia, C. Yuan and Y. Cui, *Inorg. Chem.*, 2016, **55**, 12500-12503.
15. D. R. Coulson, L. C. Satek and S. O. Grim, in *Inorg. Synth.*, John Wiley & Sons, Inc., 2007, DOI: 10.1002/9780470132449.ch23, pp. 121-124.
16. M. B. Solomon, B. Chan, C. P. Kubiak, K. A. Jolliffe and D. M. D'Alessandro, *Dalton Trans.*, 2019, **48**, 3704-3713.
17. P. M. Usov, C. Fabian and D. M. D'Alessandro, *Chem. Commun.*, 2012, **48**, 3945-3947.
18. V. A. Blatov, A. P. Shevchenko and D. M. Proserpio, *Cryst. Growth Des.*, 2014, **14**, 3576-3586.
19. G. Sheldrick, *Acta Crystallogr., Sect. A*, 2015, **71**, 3-8.
20. G. Sheldrick, *Acta Crystallogr., Sect. C*, 2015, **71**, 3-8.
21. O. V. Dolomanov, L. J. Bourhis, R. J. Gildea, J. A. K. Howard and H. Puschmann, *J. Appl. Crystallogr.*, 2009, **42**, 339-341.
22. M. Llunell, D. Casanova, J. Cicera, P. Alemany and S. Alvarez, *Journal*, 2013.
23. W. B. Jensen, *J. Chem. Educ.*, 2007, **84**, 1913.
24. M. J. Frisch, G. W. Trucks, H. B. Schlegel, G. E. Scuseria, M. A. Robb, J. R. Cheeseman, G. Scalmani, V. Barone, B. Mennucci, G. A. Petersson, H. Nakatsuji, M. Caricato, X. Li, H. P. Hratchian, A. F. Izmaylov, J. Bloino, G. Zheng, J. L. Sonnenberg, M. Hada, M. Ehara, K. Toyota, R. Fukuda, J. Hasegawa, M. Ishida, T. Nakajima, Y. Honda, O. Kitao, H. Nakai, T. Vreven, J. A. Montgomery, J. E. Peralta, F. Ogliaro, M. Bearpark, J. J. Heyd, E. Brothers, K. N. Kudin, V. N. Staroverov, R. Kobayashi, J. Normand, K. Raghavachari, A. Rendell, J. C. Burant, S. S. Iyengar, J. Tomasi, M. Cossi, N. Rega, J. M. Millam, M. Klene, J. E. Knox, J. B. Cross, V. Bakken, C. Adamo, J. Jaramillo, R. Gomperts, R. E. Stratmann, O. Yazyev, A. J. Austin, R. Cammi, C. Pomelli, J. W. Ochterski, R. L. Martin, K. Morokuma, V. G. Zakrzewski, G. A. Voth, P. Salvador, J. J. Dannenberg, S. Dapprich, A. D. Daniels, Farkas, J. B. Foresman, J. V. Ortiz, J. Cioslowski and D. J. Fox, *Journal*, 2016, DOI: citeulike-article-id:9096580.
25. J. J. P. Stewart, *J Mol Model*, 2007, **13**, 1173-1213.
26. P. J. Stephens, F. J. Devlin, C. F. Chabalowski and M. J. Frisch, *J. Phys. Chem.*, 1994, **98**, 11623-11627.
27. F. Weigend, F. Furche and R. Ahlrichs, *J. Chem. Phys.*, 2003, **119**, 12753-12762.
28. H. S. Yu, X. He, S. L. Li and D. G. Truhlar, *Chem. Sci.*, 2016, **7**, 5032-5051.
29. S. Brunauer, P. H. Emmett and E. Teller, *J. Am. Chem. Soc.*, 1938, **60**, 309-319.
30. A. V. Marenich, C. J. Cramer and D. G. Truhlar, *J. Phys. Chem. B*, 2009, **113**, 6378-6396.
31. Y. Zhao, N. E. Schultz and D. G. Truhlar, *J. Chem. Theory Comput.*, 2006, **2**, 364-382.